Supporting Information for "Evidence for an active transtensional Beaufort Range fault in the northern Cascadia forearc"

Emerson M. Lynch * [1], **Christine Regalla** [1], **Kristin Morell** [2], **Nicolas Harrichhausen** [3], **Lucinda J. Leonard** [4]

[1]School of Earth and Sustainability, Northern Arizona University, Flagstaff, AZ, USA, [2]Department of Earth Science, University of California, Santa Barbara, CA, USA, [3]Department of Geological Sciences, University of Alaska, Anchorage, AK, USA, [4]School of Earth and Ocean Sciences, University of Victoria, Victoria, BC, Canada

Contents of this file

Additional Supporting Information (Files uploaded separately)

1. Caption for large Figure S1
2. Captions for large Tables S1 to S2

Introduction

The Supporting Information contains (1) supporting text outlining lidar collection and processing, (2) supporting text outlining collection and processing methods for radiocarbon, (3) supporting text outlining methods for calculating 3D displacements, (4) supporting figures with additional examples of lidar and field observations supporting interpretations of tectonic and non-tectonic scarps, bedrock and Quaternary fault relationships, field surveys of offset geomorphic piercing lines, photos of sampled deposits, and reconstructions of local landscape evolution, and detailed fault mapping and structural measurements, and (5) supporting tables describing surficial units and radiocarbon samples, calculated displacements and slip vectors, and results of kinematic inversions.

*Corresponding author, elynch@usgs.gov; Now at U.S. Geological Survey

Text S1. Lidar processing

Lidar point cloud data were collected by Terra Remote Sensing, and provided to us by TimberWest and Island Timberlands logging companies provided ground returns. The lidar point clouds contained an average of ~1.2–1.4 ground returns per square meter. We triangulated these data into a DEM with ~0.5 m average spacing and generated topographic derivatives such as hillshade, standard deviation, and slope maps to aid in mapping.

Text S2. Geochronology methods

We determined approximate ages for mapped Quaternary deposits using radiocarbon dating of detrital charcoal. We focused our sampling on detrital charcoal as charcoal is present in many deposits on Vancouver Island, has previously been used to evaluate Late Pleistocene to Holocene unit ages (e.g., Clague et al., 1980; Morell et al., 2018; Harrichhausen et al., 2021), and because luminescence techniques have not yielded reliable ages for Late Pleistocene to Holocene deposits on Vancouver Island (e.g., Graham, 2017; Morell et al., 2018). We collected charcoal samples from natural and anthropogenic exposures of mapped Quaternary deposits to determine the chronologic ages of units offset by mapped faults (see Figure S3). We collected three macro charcoal samples and five bulk sediment samples from Site 1 (see Main Text Figure 3a for locations). Our sampling was focused on units mapped at Site 1 (Main Text Figure 3a), where we identified multiple generations of Quaternary deposits (see Section 4.2). We were unable to date any mapped deposits at Site 2 due to a lack of exposure.

Three Quaternary units yielded dateable charcoal fragments that were processed for radiocarbon analysis (Main Text Table 1, Main Text Figure 3a). The samples included macro charcoal samples extracted from one outcrop (BR-6, -7, and -8), and two samples extracted from sieved bulk sediment from two additional outcrops (BR-42 and BR-9, See Figure). Sample BR-8 was selected as the highest-quality sample of the three charcoal fragments extracted from the outcrop exposure. Bulk sediment sample BR-9 included three mm-sized charcoal pieces that were combined to ensure adequate sample mass for AMS after acid-base-acid (ABA) treatment (Main Text Table 1, Main Text Figure 3a, Figure S3). The three remaining bulk sediment samples (BR-10, -11, and -12) were barren of charcoal.

Charcoal samples were cleaned and processed at Paleotec Services, Ottawa, Ontario, Canada. Macroscopic charcoal pieces were extracted from bulk sediment samples by flotation and wet sieving in warm tap water using nested sieves of 0.85 mm and 0.425 mm. All material greater than 0.425 mm was examined using a binocular microscope, and any isolated charcoal pieces were shaved of any adhering sediment. The largest shaved fragment from each sample was further sliced into smaller fragments to look for the presence of fine modern rootlet penetration and/or fungal contamination, including mycorrhizae, and rejected if contaminants were present. Samples were analyzed at the Keck Carbon Cycle AMS Laboratory at UC Irvine. Radiocarbon ages (reported following Stuiver and Polach, 1977) were calibrated using the INTCAL20 calibration curve (Reimer et al., 2020) and OxCal v4.4 (Bronk Ramsey, 1995, 2021). We report radiocarbon ages as the 2σ range of calendar years before present (1950).

Text S3. Topographic surveys and slip reconstruction

We quantified fault slip from manual field surveying of well-preserved scarps at two key rupture sites: Site 1 and Site 2. Our primary survey targets were a series of abandoned channels and interfluves whose axes intersect fault

scarps at near-orthogonal angles, and whose topographic expressions serve as piercing lines to reconstruct fault slip vectors. Our topographic surveying methods involved physically walking out every surveyed profile in the field multiple times to be confident we were surveying the lowest point for channel thalwegs, or the highest point for interfluve crests, and ensuring the survey pole rested on true ground at each point. Topographic profiles of the targeted landforms followed either the channel thalweg or the interfluve crest. In locations where channels and interfluves were absent, we collected linear profiles with trends perpendicular to the fault scarp to calculate the vertical component of displacement (Main Text Figures 5 and 6). Each surveyed point is the average of three total station returns, typically with uncertainties less than one centimeter. This measurement uncertainty is substantially smaller than the uncertainty in our interpretation of the ground surface, due to factors such as leaf litter, moss, and tree throws.

In order to calculate a slip vector, the local orientation of the fault plane must be known. No outcrop exposures of fault planes in Quaternary deposits were present in the field area, but we instead modeled the local strike and dip of the fault plane associated with mapped scarps using a modified three-point problem approach. In this approach, we assumed the midpoint, or inflection point, of a fault scarp represents the most likely intersection of the fault plane with the surface. We surveyed scarp midpoints at multiple locations along each scarp and determined fault strike and dip through linear regression of a plane through the surveyed scarp midpoints using all surveyed data along a single continuous fault strand segment (3–17 points per regression; see Lynch et al., 2025 for script details). More variation in scarp midpoint elevations can reduce uncertainty on fault dip; we surveyed midpoints within a ∼4–12 m elevation range for each scarp segment. We used these data to determine a representative fault dip for each scarp segment, using the average dip from all regressions at Site 1 or Site 2, and a representative fault strike given by the local strike of each fault strand or segment. Because fault dips determined from surveys of degraded scarp faces over small elevation ranges may underestimate true fault dip, we set our model reconstructions to use a fault dip that is 5° steeper than that calculated from the three-point approach.

We assess uncertainty in the interpretation of what is considered a thalweg or interfluve, how these geomorphic piercing lines project into the scarp, and how the scarp has been modified within the geomorphic process zone (definition of Reitman et al., 2019) using the combined interpretations of six individuals who are each experienced in fault offset analysis. In our approach, the field surveyor and five additional individuals reviewed the survey points from offset channel thalwegs and interfluve, and selected a subset of field surveyed points that they thought best represented a straight line along each channel thalweg or interfluve crest, excluding points that appeared to be within scarp-derived colluvial wedges, eroded scarp crests, or other disturbances of the ground surface. We then calculated linear regressions and 95% confidence intervals that represent the geometry of the channel thalweg or interfluve crest on the upthrown and downthrown sides of the scarp for each of these 6 “best” interpretations. This approach allows for multiple admissible geologic slip reconstructions, whose uncertainty is typically much larger than point uncertainty (e.g., Scharer et al., 2014), and accounts for different interpretations of the width of the geomorphic fault zone (e.g., Reitman et al., 2019). This approach follows the methods of previous workers who assess uncertainty in the interpretation of offset landforms (e.g., Zielke et al., 2010; Scharer et al., 2014; Regalla et al., 2022).

We then performed offset calculations using each of these 6 interpretations of thalweg and interfluve geometry,

using a Monte Carlo simulation in a newly developed an R script to calculate 3D fault slip and uncertainty (*Script Calculating displAcements of lineaR Profiles in 3D*, or SCARP-3D; Lynch et al., 2025). The SCARP-3D code accounts both for uncertainty on the geometry of the offset landform and uncertainty in fault geometry. Each simulation calculates the 3D offset of a geomorphic piercing line by randomly selecting a linear regression for the upthrown and downthrown piercing lines from the 95% confidence intervals for each linear regression, and randomly selecting a fault plane geometry from the 2σ uncertainty of fault strike and dip determined from the 3-point calculations described above.

The SCARP-3D code requires the following user-defined inputs: the strike and dip of the fault plane and the 1σ uncertainty (5°) on strike and dip, the XYZ coordinates of the topographic profile data, the location where the fault plane intersects the ground surface, and the number of points in the upthrown and downthrown sides of the profile used to define the 3D geometry of the piercing line segments from each of the five individuals' selections. We manually defined the remaining parameters—the point where the fault plane intersects the ground surface, and the individual points used to fit linear regressions through the upthrown and downthrown piercing line profiles—for each topographic profile.

Using these inputs, we used SCARP-3D to calculate 3D linear regressions through topographic profiles on the upthrown and downthrown sides of the fault scarp and then solve for the intersection points of the linear regressions with the fault plane (Main Text Figure 8). The two intersection points were then used to calculate the magnitudes of strike slip (SS), dip slip (DS), and oblique slip (OS) for each piercing line, as well as the trend and plunge of the slip vector (Main Text Figure 8). SCARP-3D repeats a Monte Carlo simulation 100 times for each of the six user-defined profile selections as well as for all field-surveyed points, yielding a total of 600 simulations of fault slip for each displaced piercing line. We report uncertainties on all offset measurements as the mean and standard deviation calculated from all 600 offset measurements per piercing line (Main Text Figure 9; Table S2).

References

Bronk Ramsey, C. Radiocarbon calibration and analysis of stratigraphy: The OxCal program. *Radiocarbon*, 37(2):425–430, 1995. doi: 10.1017/s0033822200030903.

Bronk Ramsey, C. OxCal Program, Version 4.4, 2021.

Clague, J. J., Armstrong, J. E., and Mathews, W. H. Advance of the late Wisconsin Cordilleran Ice Sheet in southern British Columbia since 22,000 Yr B.P. *Quaternary Research*, 13(3):322–326, 1980. doi: 10.1016/0033-5894(80)90060-5.

Cui, Y., Miller, D., Schiarizza, P., and Diakow, L. British Columbia digital geology. Technical Report 2017-8, British Columbia Ministry of Energy, Mines and Petroleum Resources, 2017.

Fyles, J. G. Surficial geology of Horne Lake and Parksville map-areas, Vancouver Island, British Columbia. *Geological Survey of Canada Memoir*, 318:142, 1963.

Graham, A. Geometry, kinematics, and Quaternary activity of the Leech River fault zone, southern Vancouver Island, British Columbia, Canada. Master's thesis, University of Victoria, 2017.

Harrichhausen, N., Morell, K. D., Regalla, C., Bennett, S. E., Leonard, L. J., Lynch, E. M., and Nissen, E. Paleoseismic trenching reveals Late Quaternary kinematics of the Leech River fault: implications for forearc strain accumulation in northern Cascadia. *Bulletin of the*

Seismological Society of America, 111(2):1110–1138, 2021. doi: 10.1785/0120200204.

JPL, N. NASA Shuttle Radar Topography Mission Global 1 arc second, 2013. doi: 10.5067/MEaSUREs/SRTM/SRTMGL1.003. Dataset.

Li, Z., Bruhn, R. L., Pavlis, T. L., Vorkink, M., and Zeng, Z. Origin of sackung uphill-facing scarps in the Saint Elias orogen, Alaska: LIDAR data visualization and stress modeling. *Bulletin of the Geological Society of America*, 122(9-10):1585–1589, 2010. doi: 10.1130/B30019.1.

Lynch, E. M., Regalla, C., Morell, K. D., Harrichhausen, N., and Leonard, L. J. Three-dimensional offsets of geomorphic piercing lines displaced by the Quaternary-active Beaufort Range fault, northern Cascadia forearc, BC, Canada, 2025. doi: https://doi.org/10.5061/dryad.nvx0k6dvc. Dataset.

Morell, K. D., Regalla, C., Amos, C. B., Bennett, S. E., Leonard, L. J., Graham, A., Reedy, T., Levson, V., and Telka, A. Holocene surface rupture history of an active forearc fault redefines seismic hazard in southwestern British Columbia, Canada. *Geophysical Research Letters*, 45 (21):11,605–11,611, 2018. doi: 10.1029/2018GL078711.

Regalla, C., Kirby, E., Mahan, S., McDonald, E., Pangrcic, H., Binkley, A., Schottenfels, E., LaPlante, A., Sethanant, I., and Lynch, E. M. Late Holocene rupture history of the Ash Hill fault, Eastern California Shear Zone, and the potential for seismogenic strain transfer between nearby faults. *Earth Surface Processes and Landforms*, 47(12):2897–2925, 2022.

Reimer, P. J., Austin, W. E., Bard, E., Bayliss, A., Blackwell, P. G., Bronk Ramsey, C., Butzin, M., Cheng, H., Edwards, R. L., Friedrich, M., Grootes, P. M., Guilderson, T. P., Hajdas, I., Heaton, T. J., Hogg, A. G., Hughen, K. A., Kromer, B., Manning, S. W., Muscheler, R., Palmer, J. G., Pearson, C., Van Der Plicht, J., Reimer, R. W., Richards, D. A., Scott, E. M., Southon, J. R., Turney, C. S., Wacker, L., Adolphi, F., Büntgen, U., Capano, M., Fahrni, S. M., Fogtmann-Schulz, A., Friedrich, R., Köhler, P., Kudsk, S., Miyake, F., Olsen, J., Reinig, F., Sakamoto, M., Sookdeo, A., and Talamo, S. The IntCal20 Northern Hemisphere radiocarbon age calibration curve (0-55 cal kBP). *Radiocarbon*, 62(4):725–757, 2020. doi: 10.1017/RDC.2020.41.

Reitman, N. G., Mueller, K. J., Tucker, G. E., Gold, R. D., Briggs, R. W., and Barnhart, K. R. Offset channels may not accurately record strike-slip fault displacement: Evidence from landscape evolution models. *Journal of Geophysical Research: Solid Earth*, 124(12):13427–13451, 2019. doi: 10.1029/2019JB018596.

Rogers, G. C. Earthquake fault plane solutions near Vancouver Island. *Canadian Journal of Earth Sciences*, 16(3):523–531, 1979. doi: 10.1139/e79-047.

Rogers, G. C. and Hasegawa, H. S. A second look at the British Columbia earthquake of June 23, 1946. *Bulletin of the Seismological Society of America*, 68(3):653–676, 1978.

Scharer, K., Salisbury, J., Arrowsmith, R., and Rockwell, T. Southern San Andreas fault evaluation field activity: approaches to measuring small geomorphic offsets–challenges and recommendations for active fault studies. *Seismological Research Letters*, 85:68–76, 2014. doi: 10.1785/0220130108.

Stuiver, M. and Polach, H. A. Reporting of ^{14}C data. *Radiocarbon*, 19(3):355–363, 1977.

Zielke, O., Arrowsmith, J. R., Ludwig, L. G., and Akçiz, S. O. Slip in the 1857 and earlier large earthquakes along the Carrizo Plain, San Andreas Fault. *Science*, 327(5969):1119–1122, 2010. doi: 10.1126/science.1182781.

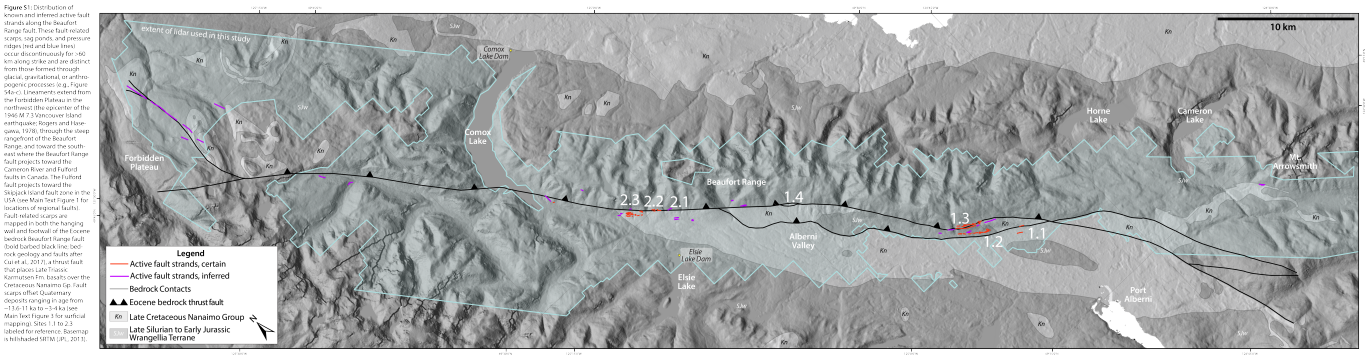

Figure S1 High-resolution map of known and inferred scarps associated with active fault strands along the Beaufort Range fault. These fault-related scarps, sag ponds, and pressure ridges (red and blue lines) occur discontinuously for >35 km along strike (100 km including potentially tectonic scarps identified from lidar alone) and are distinct from those formed through glacial, gravitational, or anthropogenic processes (e.g., Figure S4a-c). Lineaments extend from the Forbidden Plateau in the northwest (the epicenter of the 1946 M 7.3 Vancouver Island earthquake; Rogers, 1979), through the steep rangefront of the Beaufort Range, and toward the southeast where the Beaufort Range fault projects toward the Cameron River and Fulford faults in Canada. The Fulford fault projects toward the Skipjack Island fault zone in the USA (see Main Text Figure 1 for locations of regional faults). Fault-related scarps are mapped in both the hanging wall and footwall of the Eocene bedrock Beaufort Range fault (bold barbed black line; bedrock geology and faults after Cui et al., 2017), a thrust fault that places Late Triassic Karmutsen Fm. basalts over the Cretaceous Nanaimo Gp. Fault scarps offset Quaternary deposits ranging in age from ∼13.6–11 ka to ∼3–4 ka (see Main Text Figure 3 for surficial mapping). Basemap is hillshaded SRTM DEM (JPL, 2013). *Full-resolution Figure S1 can be downloaded as a separate file.*

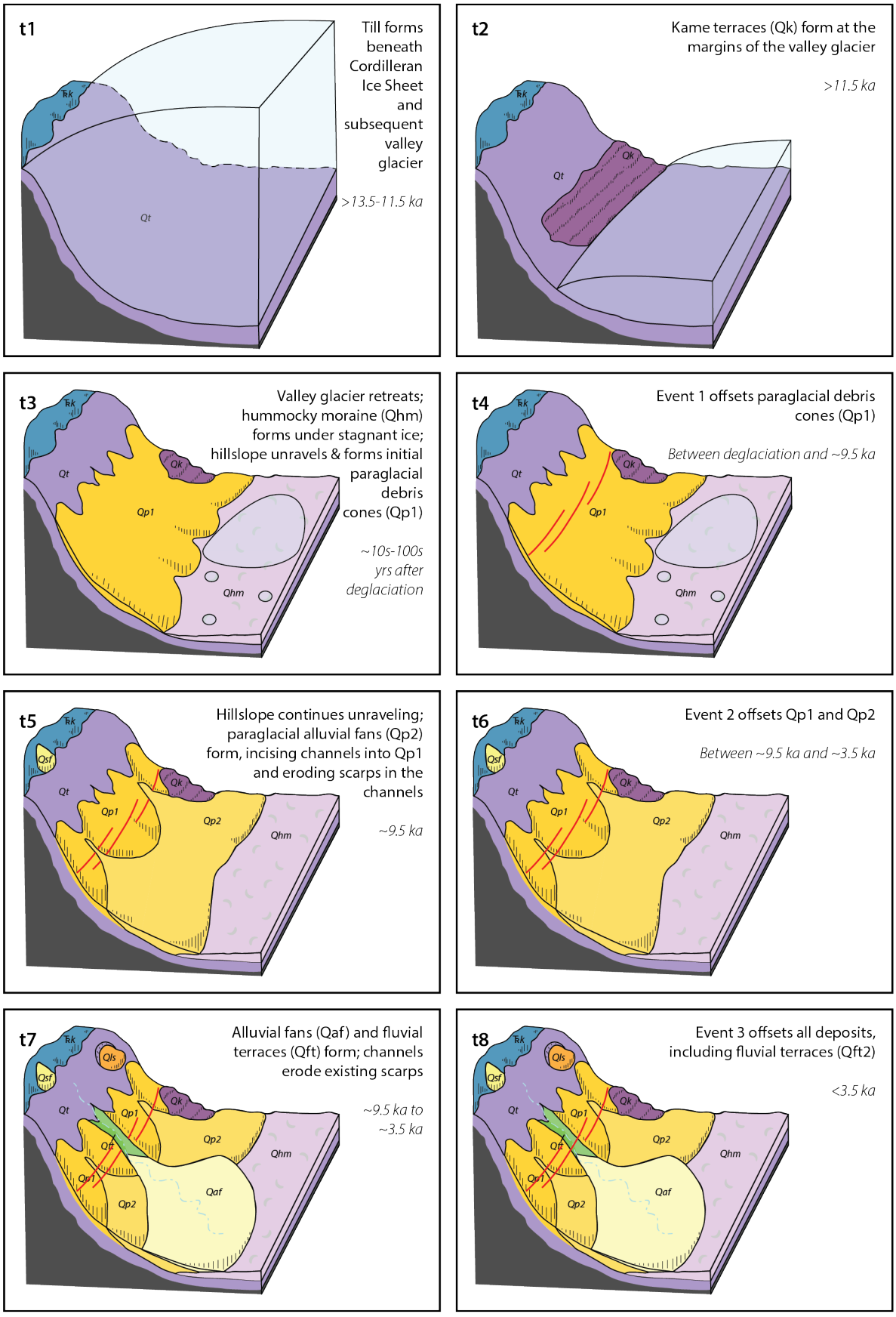

Figure S2 Schematic showing landscape evolution and formation of surficial deposits along the Beaufort Range from the Cordilleran glaciation (t0) through Event 3 (t8).

Figure S3 ***(following page)*** Photos of radiocarbon sample locations and surrounding deposits. Qp1 - Late Pleistocene to Early Holocene paraglacial deposits, old; Qp2 - Late Pleistocene to Early Holocene paraglacial deposits, middle; Qaf - Middle to Late Holocene alluvial fans and associated terraces; Qft - Late Pleistocene to Holocene fluvial terraces. Main Text Figure 3 shows the locations of dated samples. **a:** Alluvial fan (Qaf) exposure in modern stream channel where samples BR-6, -7 and -8 were collected. Deposit consists of interbedded cobbles and gravels with some finer sand beds and lenses. Beds are roughly horizontal and clast supported, with sub-angular to sub-rounded clasts. The matrix is similar throughout, red-brown with a muddy composition, likely composed of Fe oxides with clay and sands. The alluvial fan unit is 2–3 m thick and topped by a fluvial deposit, overlain by colluvium. **b:** Close-up of the location in panel a showing the individual sample locations within the Qaf deposit. Samples BR-6, -7, and -8 were collected from a $\sim$1 m wide by 30–40 cm thick lens of pebbles and coarse sands, $\sim$1 m above the active channel floor, $\sim$2 m below the fan surface. **c:** Sample BR-6 in situ. **d:** Sample BR-7 in situ. **e:** Sample BR-8 in situ. **f:** Road cut exposure where sample BR-10 was collected from an indurated coarse sand lens (outlined in red) within stratified sands and gravels (Qp2). **g:** Roadside exposure where sample BR-11 was collected from sandy interbeds outlined in red (Qp1). Colluvium and detritus on the surface was removed, and the bulk sediment sample was collected from freshly exposed sediments. **h:** Paraglacial deposit exposure (Qp1) where sample BR-12 was collected. Qp1 was very indurated, and required hammering to collect bulk sediment (area sampled outlined in red). **i:** Roadside exposure where sample BR-9 was collected. Colluvium and detritus on the surface was removed, and the bulk sediment sample was collected from freshly exposed Qp2 sediments (outlined in red). **j:** Fluvial terrace (Qft) exposure in modern stream channel where sample BR-42 was collected from a pebble bed (outlined in red). The cobble lens indicated in yellow was plucked out prior to sampling due to an abundance of plant litter.

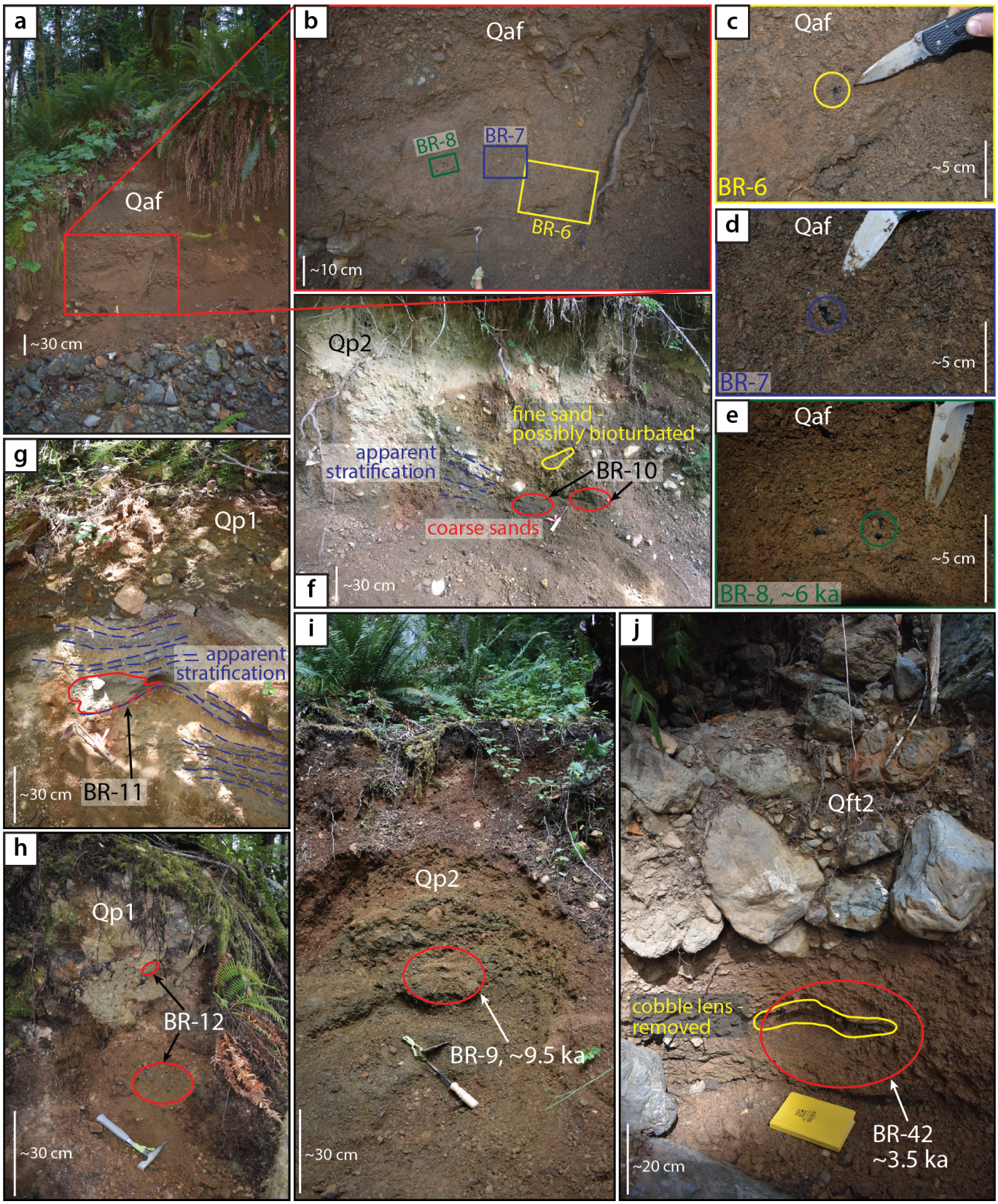
a
Qaf
~30 cm
b
Qaf
BR-8
BR-7
BR-6
~10 cm
c
Qaf
BR-6
~5 cm
d
Qaf
BR-7
~5 cm
e
Qaf
BR-8, ~6 ka
~5 cm
f
Qp2
fine sand - possibly bioturbated
apparent stratification
BR-10
coarse sands
~30 cm
g
Qp1
apparent stratification
BR-11
~30 cm
h
Qp1
BR-12
~30 cm
i
Qp2
BR-9, ~9.5 ka
~30 cm
j
Qft2
cobble lens - removed
BR-42 ~3.5 ka
~20 cm

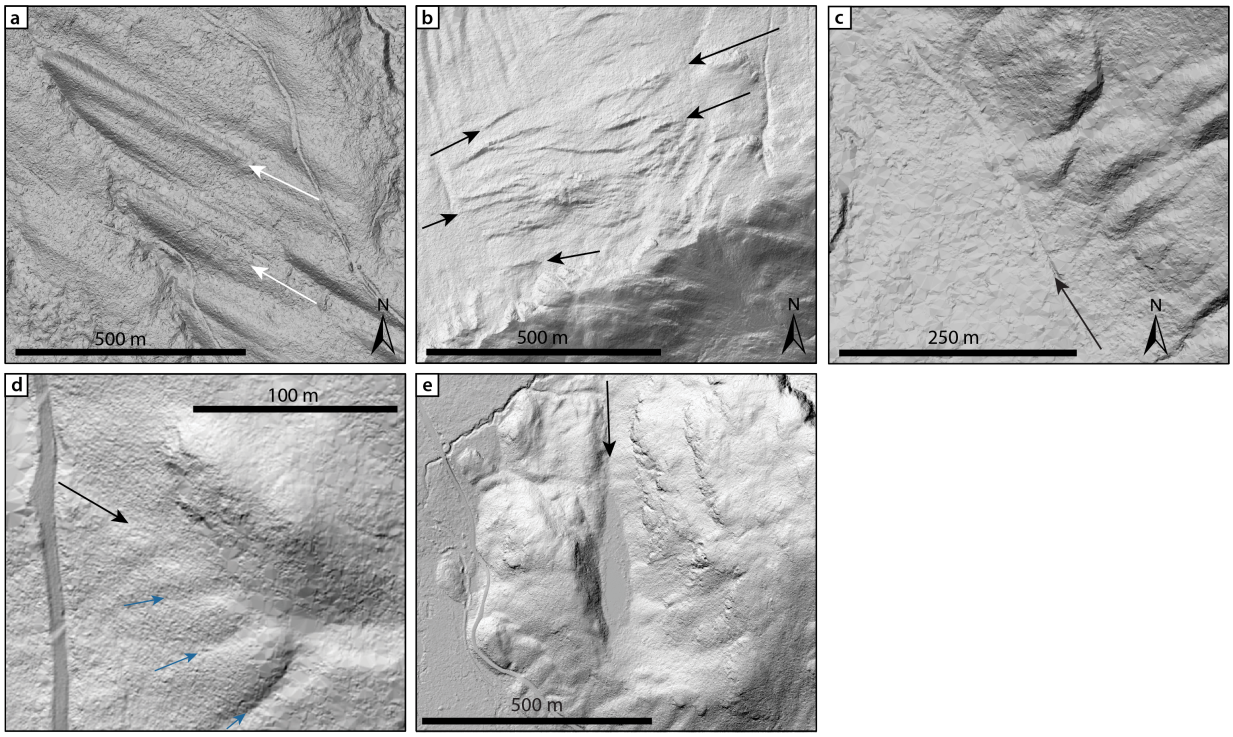

Figure S4 Hillshaded lidar DEMs showing examples of non-tectonic (panels a-c) and tectonic (panels d and e) lineaments along the Beaufort Range. **a:** White arrows indicate streamlined glacial drumlins and lineaments. These lineaments trend down-valley toward ~120°, sub-parallel to the valley glacier flow direction of Fyles (1963). **b:** Black arrows indicate sackungen, parallel linear scarps near ridge crests associated with gravitational failures after retreat of a glacial buttress (e.g., Li et al., 2010). **c:** Black arrow indicates a decommissioned logging road. The uphill side (right) is carved out, while the downhill side (left) is oversteepened due to deposition of excess material during road building. **d:** Black arrow points to a "bench," or a flat, degraded topographic feature embedded in the high-gradient hillslope, that truncates several paleochannels (blue arrows). **e:** A linear depression developed in Karmutsen Fm. basalt that collects water (a sag pond), the trend of which is oblique to the range front.

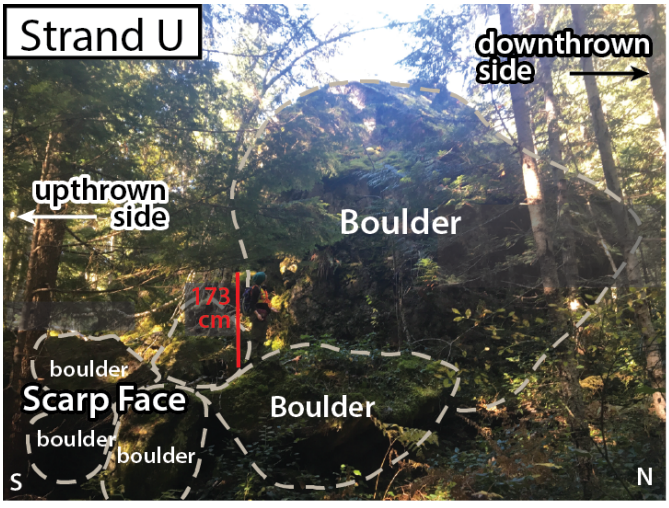

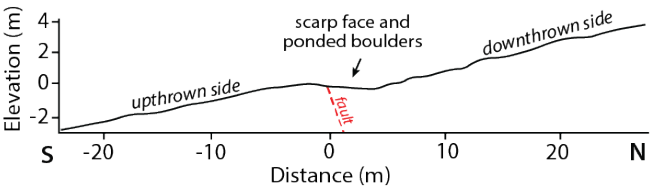

Figure S5 Field photo and topographic profile of a fault scarp (Strand U) at Site 2.3. **a:** Photograph showing large boulders (~1.5–8 m; outlined in dashed gray) ponded against fault scarp U at Site 2.3. See Main Text Figures 3 and 6 for location. **b:** Topographic profile across strand U.

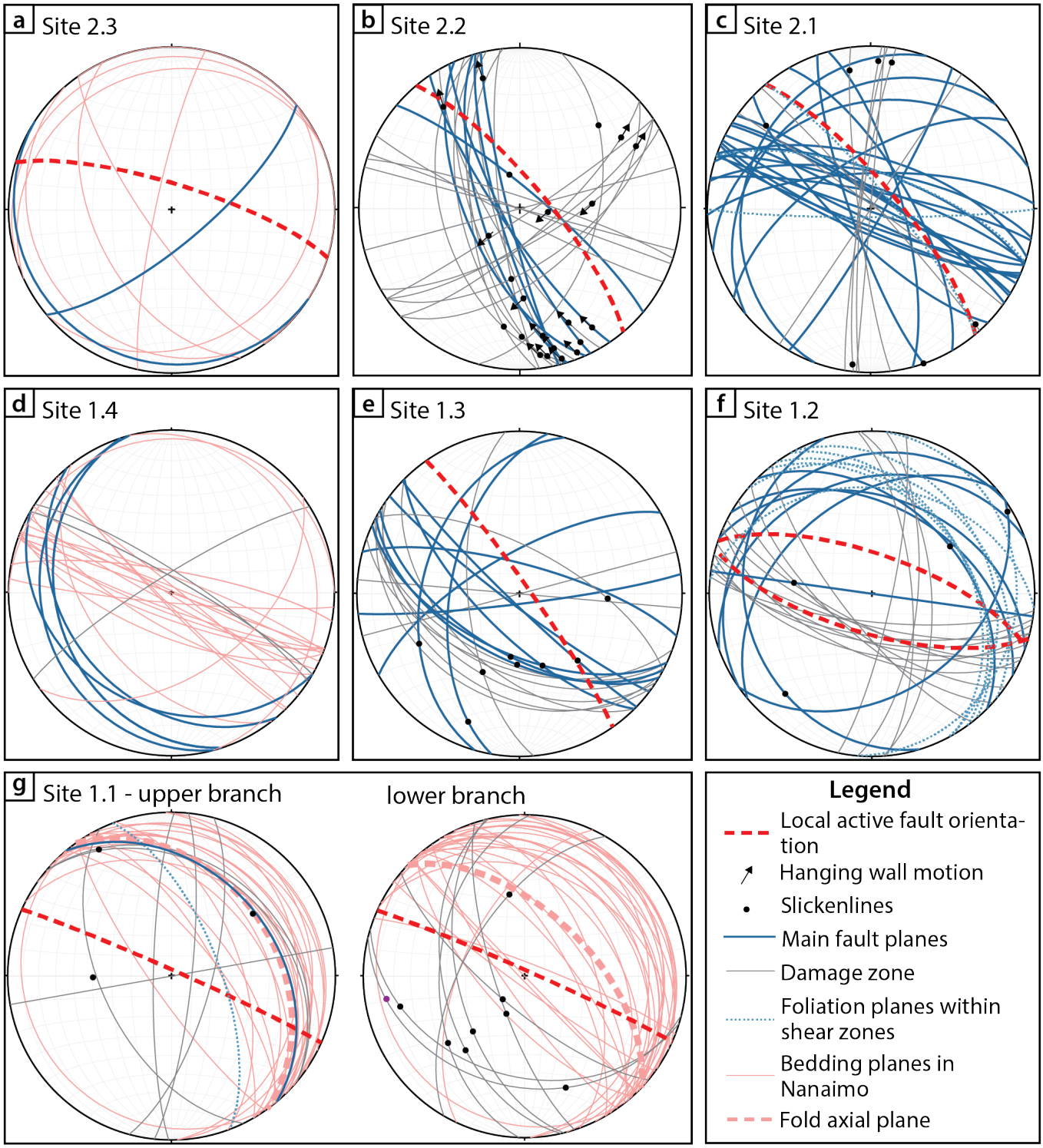

Figure S6 Lower hemisphere equal-area projections showing structural measurements in bedrock at Sites 2.3–1.2 (presented northwest to southeast; see Main Text Figure 3 and Figure S1 for locations). **a:** At Site 2.3, bedrock faults and bedding planes are mostly gently dipping, in contrast with the active fault that is steeply dipping. Steeply-dipping bedding at Site 2.3 is part of the upturned limb of a syncline in the footwall of the Eocene bedrock thrust fault. **b:** At Site 2.2, bedrock fault planes have similar dip magnitudes to the active fault, but opposite dip directions. Slickenlines and Riedel shear orientations (light gray) at Site 2.2 primarily record right-lateral, NE-up motion. **c:** At Site 2.1, the majority of bedrock fault planes are $\sim$20° oblique to the active fault strike. **d:** Site 1.4 is an exposure of Nanaimo bedding in a footwall syncline. **e:** At Site 1.3, bedrock fault planes primarily dip SW, and strikes are $>$10° apart from the active fault orientation. **f:** Site 1.2 records gently-dipping foliation and main bedrock fault planes, in contrast to steeply-dipping active fault planes. **g:** Site 1.1 records two footwall synclines in Nanaimo Gp., related to the two branches of the Eocene bedrock thrust fault (see Main Text Figure 3a). Our measurements of Nanaimo Gp. bedding at this site suggest the axes of these footwall synclines are located very near the fault traces.

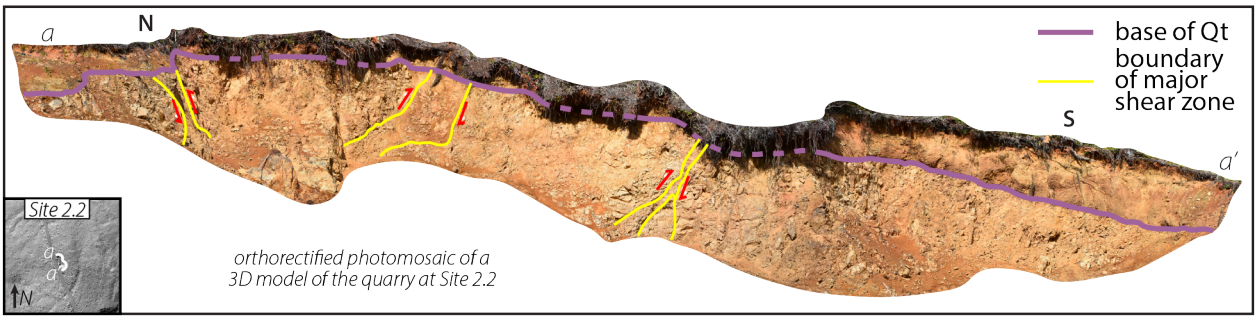

Figure S7 Quaternary till (Qt) deposited smoothly over the Eocene bedrock thrust fault zone at Site 2.2. The lack of offset in Qt across the fault demonstrates that the Eocene bedrock thrust fault has not been active in the Quaternary.

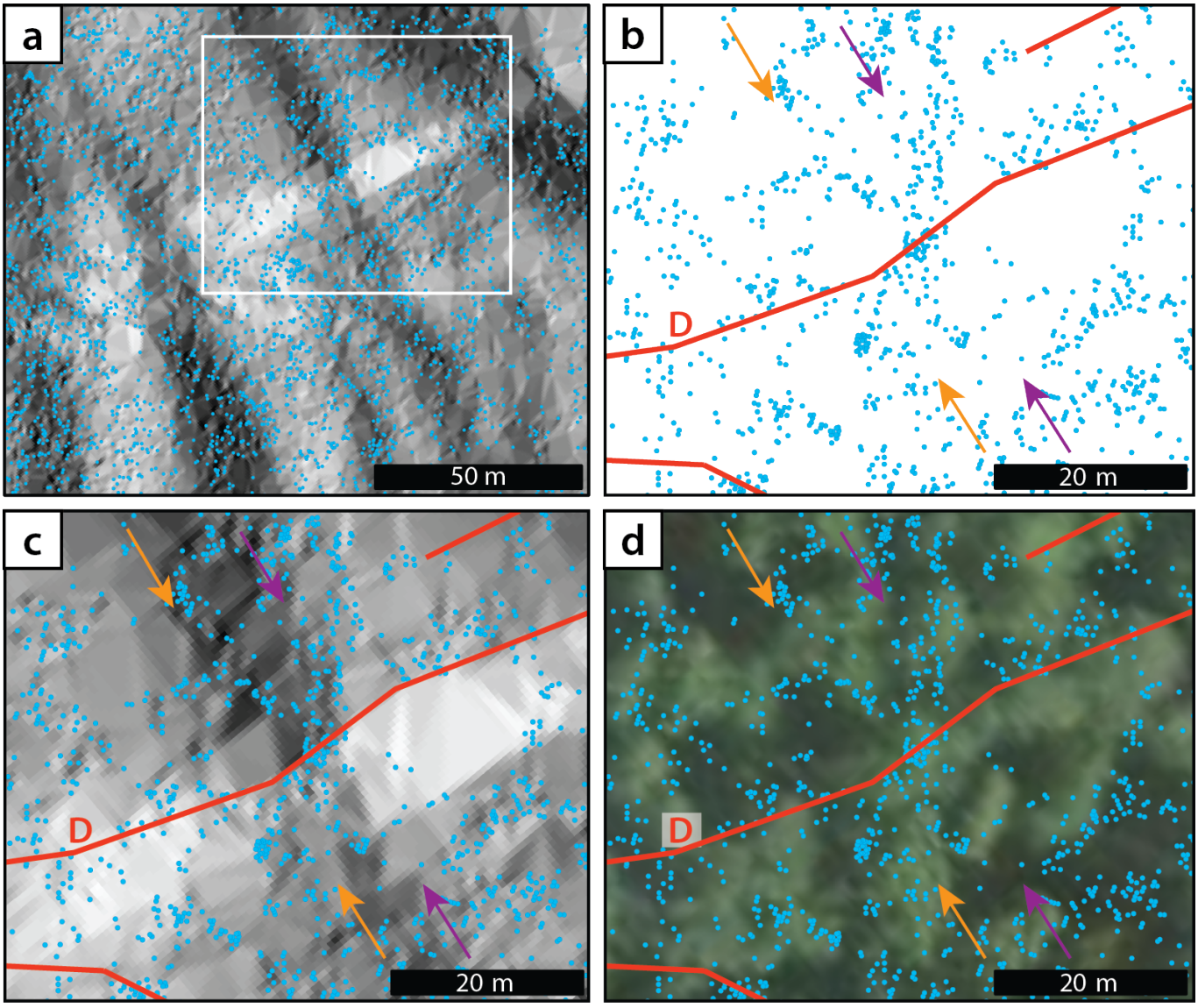

Figure S8 Example of non-uniform lidar ground return spacing in areas containing fault scarps. **a**. Lidar ground returns (blue dots) over lidar-derived hillshaded DEM for Site 1.2. White box shows location of panels b-d. **b.** Inset map showing the positions of lidar ground returns. Note the sparse ground returns in the vicinity of fault strands (red lines), an offset interfluve crest (orange arrow), and an offset channel thalweg (purple arrow). **c.** Same data as in panel b, overlain on lidar-derived hillshaded DEM. **d.** Same data as in panel b, overlain on ArcGIS satellite image base map. Ground returns are often absent within tree canopy centers, and instead occur at crown margins. Due to irregular spacing and large gaps between ground returns, combined with false returns on downed logs and other forest floor litter, topographic contours across lidar generated DEMs do not necessarily match topographic forms observable in the field. As a result, measurements of offset of topographic piercing lines are based on field observations and surveys, rather than lidar DEM analyses.

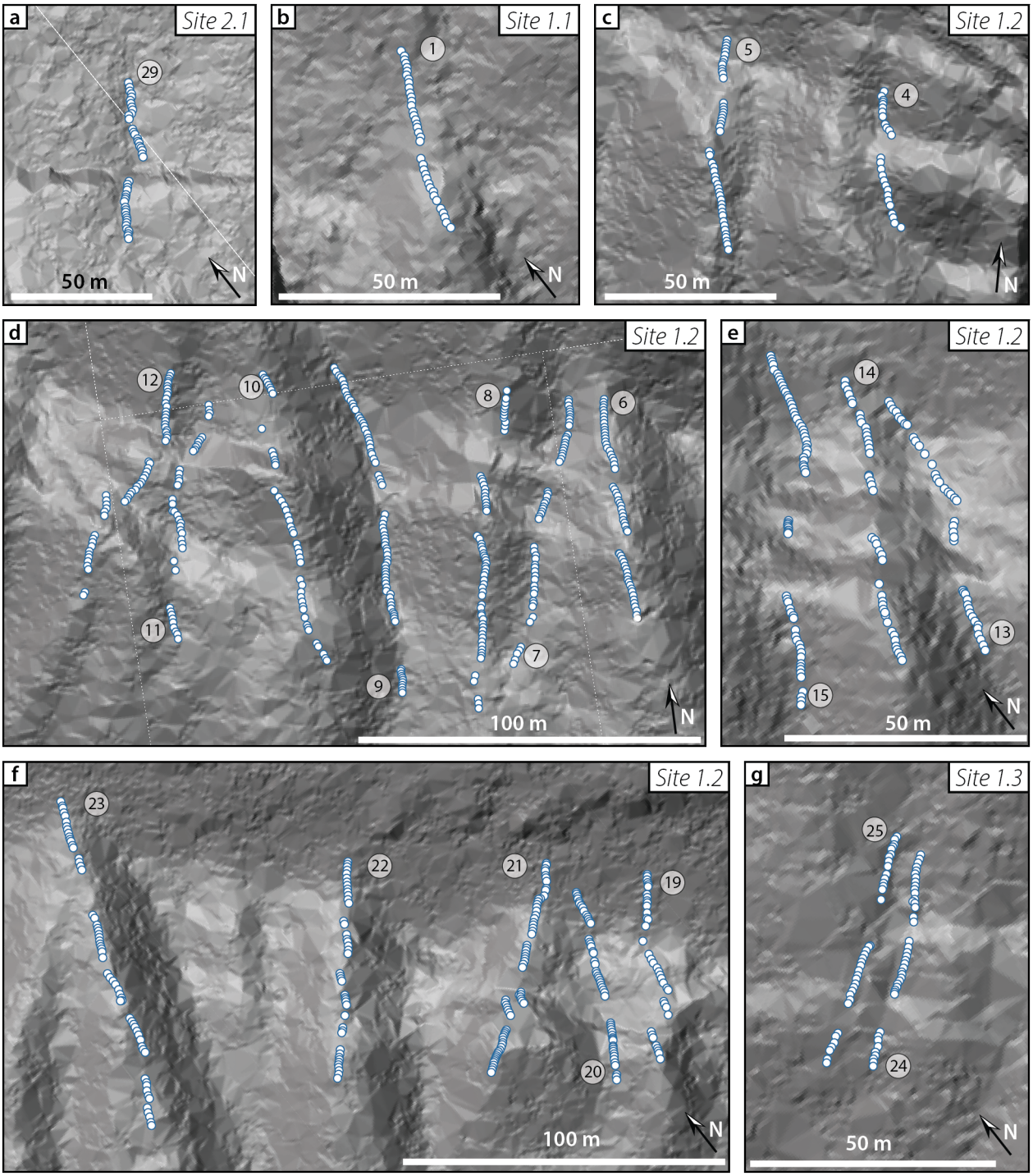

Figure S9 Surveyed topographic profiles of interfluve crests and channel thalweg across the Beaufort Range fault, shown over lidar-derived slopeshade (TIN). Individual survey points are shown as blue outlined dots. Profiles 16, 17, and 18 are shown in Main Text Figure 4. We note that due to poor lidar DEM resolution in the densely vegetated survey area, field surveys positions of interfluve crests and channel thalwegs may not always align with the apparent thalwegs and interfluve crests visible in the shaded elevation model. Offsets associated with these profiles are provided in table Table S2.

Table S1 Sediment and surface morphology descriptions of units mapped in Main Text Figure 3. *Table S1 can be downloaded as a separate file.*

Table S2 BRF displacements and slip vectors determined from reconstructions of offset geomorphic piercing lines. *Table S2 can be downloaded as a separate file.*

169

Table S3 Nodal planes and P- and T-axis orientations for the 1946 Vancouver Island earthquake, and for kinematic inversions of BRF displacement data.

Solution	Nodal Plane 1 (strike/dip)	Nodal Plane 2 (strike/dip)	P-axis (trend/plunge)	T-axis (trend/plunge)	Slip vector (trend/plunge)[a]
1946 focal mechanism A[b]	319/79 NE	228/85 N	183/12	274/05	183/05
1946 focal mechanism B[b]	332/66 NE	233/70 NW	191/32	283/02	143/20
1946 focal mechanism C[b]	330/67 NE	222/36 NW	198/58	080/17	114/54
Site 2.3[c]	276/78 N	181/64 W	141/27	046/09	096/10
Site 1.3[c]	321/75 NE	199/26 NW	204/54	068/27	135/26
Site 1.2[c]	292/66 NE	160/34 SW	165/61	040/17	107/15
Site 1.1[c]	294/75 NE	187/43 W	164/45	053/20	109/19
All Sites[c]	296/83 NE	199/43 NW	170/37	058/26	109/48

[a] Calculated slip vector along NW-SE striking plane

[b] Focal mechanism solutions for the 1946 Vancouver Island earthquake (Rogers and Hasegawa, 1978)

[c] FaultKin inversions for the Beaufort Range fault, from offset piercing lines, this study